Journal of Materials Chemistry A

PAPER

View Article Online
View Journal | View Issue

Cite this: J. Mater. Chem. A, 2015, 3, 22886

MoS_2 nanosheet-coated CoS_2 nanowire arrays on carbon cloth as three-dimensional electrodes for efficient electrocatalytic hydrogen evolution†

Jilin Huang,[a] Dongman Hou,[b] Yucheng Zhou,[a] Weijia Zhou,*[a] Guoqiang Li,[b] Zhenghua Tang,[a] Ligui Li[a] and Shaowei Chen*[ac]

Received 10th September 2015
Accepted 2nd October 2015

DOI: 10.1039/c5ta07234d

www.rsc.org/MaterialsA

The design and engineering of low-cost and high-efficiency electrocatalysts for the hydrogen evolution reaction (HER) has attracted increasing interest in renewable energy research. Herein, MoS_2 nanosheet-coated CoS_2 nanowire arrays supported on carbon cloth (MoS_2/CoS_2/CC) were prepared by a two-step procedure that entailed the hydrothermal growth of $Co(OH)_2$ nanowire arrays on carbon cloth followed by reaction with $(NH_4)_2MoS_4$ to grow an overlayer of MoS_2 nanosheets. Electrochemical studies showed that the obtained 3D electrode exhibited excellent HER activity with an overpotential of −87 mV at 10 mA cm^{-2}, a small Tafel slope of 73.4 mV dec^{-1} and prominent electrochemical durability. The results presented herein may offer a new methodology for the design and engineering of effective multilevel structured catalysts for the HER based on earth-abundant components.

Introduction

Hydrogen has been hailed as a sustainable, secure, and clean alternative energy source that may satisfy the growing global energy demand. Yet, such a promise will be realized only when the production of hydrogen can be carried out in an efficient, low-cost, and environmentally friendly fashion. An electrocatalytic hydrogen evolution reaction (HER) is a highly attractive means for meeting these requirements.[1–3] Among the various HER electrocatalysts, noble metals such as Pt have been the catalysts of choice thus far, but scarcity and high costs have severely limited their practical applicability.[4–7] In recent years, a great deal of research effort has been devoted to using earth abundant and inexpensive materials to replace Pt as HER electrocatalysts, including transition metal sulfides,[1,7–11] selenides,[12] carbides,[13–15] and phosphides.[16–20] Among these, MoS_2 has received particular attention due to the earth-abundant composition and high activity.[21–28] Yet, with the anisotropic structure of the sandwiched S–Mo–S layers, MoS_2 is prone to form a two-dimensional (2D) morphology leading to a limited number of active sites for the HER.

The catalytic performance may be further improved by doping other atoms into the catalysts by manipulation of the hydrogen adsorption energy. In fact, a variety of transition metal or non-metal atoms have been used as dopants, such as Co, Ni, Li, N, Cl and O.[21,29–34] For example, the Dai group reported the synthesis of highly active and stable hybrid electrocatalysts for the HER based on Co-doped iron pyrite (FeS_2) supported on carbon nanotubes ($Fe_{1-x}Co_xS_2$/CNT), which achieved a low overpotential of −0.12 V at 20 mA cm^{-2}, a Tafel slope of 46 mV dec^{-1}, and excellent stability over 40 h in acidic solution.[35] Xie and coworkers demonstrated the synergistic regulation of both structural and electronic benefits of controllable disorder engineering and simultaneous O atom incorporation into MoS_2, and observed dramatically enhanced HER activity.[30]

Moreover, with increasing roughness of the electrode, one anticipates to see a decrease of the electrode size and an increase of the number of catalytic sites available for the HER. Within this context, nanowire arrays integrated with a conducting substrate may enjoy the additional advantages of both charge carrier transport and the release of evolved hydrogen gas from the electrode surface.[36–38] Note that cobalt pyrite (CoS_2) has been reported to be catalytically active for the HER with metal-like conductivity.[39] Therefore, CoS_2 nanowire arrays may be an ideal three-dimensional (3D) conductive substrate that features high HER activity.

In order to meet the above requirements (a high electrochemical active area, high conductivity and abundant catalytic active sites), we designed and synthesized an HER electrode based on a hybrid structure consisting of CoS_2 nanowires coated with cobalt and oxygen co-doped MoS_2 nanosheets on carbon

[a]New Energy Research Institute, School of Environment and Energy, South China University of Technology, Guangzhou Higher Education Mega Center, Guangzhou, Guangdong 510006, China. E-mail: eszhouwj@scut.edu.cn

[b]State Key Laboratory of Luminescent Materials and Devices, South China University of Technology, 381 Wushan Road, Guangzhou 510641, China

[c]Department of Chemistry and Biochemistry, University of California, 1156 High Street, Santa Cruz, California 95064, USA. E-mail: Shaowei@ucsc.edu

† Electronic supplementary information (ESI) available: Additional experimental data and discussion, Fig. S1–S4. See DOI: 10.1039/c5ta07234d

cloth (MoS_2/CoS_2/CC). The resulting nanocomposites exhibited remarkable HER stability and activity. Experimentally, CoS_2 nanowire arrays were used as 3D electrodes to obtain a high electrochemically active surface area. Cobalt and oxygen co-doped MoS_2 nanosheets were then concurrently grown on the CoS_2 nanowire surface. The obtained MoS_2/CoS_2 hybrids exhibited a low overpotential of only −87 mV at 10 mA cm^{-2}, a small Tafel slope of 73.4 mV dec^{-1}, and good catalytic stability.

Experimental section

Chemicals

All reagents were of analytical grade and used without further purification. Ammonium tetrathiomolybdate ($(NH_4)_2MoS_4$), sodium sulfide (Na_2S), cobalt chloride ($CoCl_2 \cdot 6H_2O$), ammonium chloride (NH_4Cl), carbamide ($CO(NH_2)_2$), 20 wt% Pt/C, and carbon cloth (CC) were obtained from Sinopharm Chemical Reagents Beijing Co. and used as received. Water was supplied with a Barnstead Nanopure Water System (18.3 MΩ cm).

Synthesis of $Co(OH)_2$ nanowires supported on CC

In a typical reaction, 0.29 g of $CoCl_2 \cdot 6H_2O$, 0.92 g of NH_4Cl, and 0.37 g of $CO(NH_2)_2$ were dissolved in 20 mL of Nanopure water under vigorous stirring for 30 min. Then the solution was transferred into a Teflon-lined stainless autoclave (25 mL) and a piece of CC (3.5 cm × 2.2 cm; which was cleaned by ultrasonication in acetone, ethanol and water for 20 min each prior to use). The autoclave was sealed and heated at 120 °C for 6 h in an electric oven, and then air-cooled to room temperature. The carbon cloth was taken out and washed with water before being dried at 70 °C for 6 h, affording $Co(OH)_2$ nanowires supported on CC which were denoted as $Co(OH)_2$/CC.

Synthesis of MoS_2/CoS_2 heterostructures on carbon cloth (MoS_2/CoS_2/CC)

Experimentally, 50 mg of $(NH_4)_2MoS_4$ was dissolved in 20 mL of Nanopure water to form a solution. Then the solution was transferred into a Teflon-lined stainless autoclave (25 mL) and a piece of $Co(OH)_2$/CC prepared above (2 cm × 0.5 cm) was immersed into the solution. The autoclave was heated at 200 °C for 24 h. The resulting MoS_2/CoS_2/CC (at a loading of about 18.6 mg cm^{-2}) was harvested after being washed with water thoroughly and vacuum dried.

CoS_2/CC (at a loading of about 16.5 mg cm^{-2}) was synthesized in a similar fashion but by using 50 mg of Na_2S instead of $(NH_4)_2MoS_4$. Another sample, MoS_2/CC (at a loading of about 4.2 mg cm^{-2}), was prepared also by the same procedure where pristine CC (2 cm × 0.5 cm) was used instead of CoS_2/CC.

Characterization

Scanning electron microscopy (SEM) analysis was carried out with a FEI NOVA NanoSEM 430 field-emission microscope. Transmission electron microscopy (TEM) measurements were carried out with a JOEL JEM 2100F microscope. Powder X-ray diffraction (XRD) patterns of the samples were recorded on a Bruker D8 Advance powder X-ray diffractometer with Cu Kα (λ = 0.15406 nm) radiation. X-ray photoelectron spectroscopy (XPS) measurements were performed using a PHI X-tool instrument (Ulvac-Phi). Raman spectra were recorded on a RENISHAW inVia instrument with an Ar laser source of 488 nm in a macroscopic configuration.

Electrochemistry

Electrochemical measurements were performed with an electrochemical workstation (CHI 760C, CH Instruments Inc.) in a 0.5 M H_2SO_4 aqueous solution. A saturated calomel electrode (SCE, sat'd KCl) and platinum plate were used as the reference and counter electrodes, respectively. The MoS_2/CoS_2/CC prepared above was used directly as a binder-free working electrode. The current densities were evaluated in terms of the geometrical surface area of MoS_2/CoS_2/CC. Polarization curves were acquired by sweeping the potential from 0 to −0.5 V (*vs.* RHE) at a potential sweep rate of 5 mV s^{-1}. Electrochemical impedance spectroscopy (EIS) was carried out with an amplitude of 10 mV and frequency range from 100 kHz to 0.01 Hz. The main arc in each EIS spectrum was fitted using a simplified Randles equivalent circuit, which consisted of an uncompensated resistance (R_s) in series with a parallel arrangement of a charge-transfer resistance (R_{ct}) and a constant phase element (CPE), and the fitting parameters were estimated through the application of the Levenberg–Marquardt minimization procedure. Cyclic voltammetry (CV) was used to probe the electrochemical double layer capacitance at nonfaradaic potentials as a means to estimate the effective electrode surface area. Accelerated stability tests were performed in 0.5 M H_2SO_4 at room temperature by potential cycling between 0 and −0.4 V (*vs.* RHE) at a sweep rate of 100 mV s^{-1} for a given number of cycles. Current–time responses were monitored by chronoamperometric measurements. The hydrogen gas production rate was quantified by gas chromatographic measurements (GC-2060F, LuNan Analytical Instruments, LTD, China).

Results and discussion

Hierarchical MoS_2/CoS_2 arrays were synthesized by using $Co(OH)_2$ nanowires as a hard template (Fig. S1†). During the hydrothermal reaction, $(NH_4)_2MoS_4$ was decomposed into MoS_2 nanosheets and deposited on the surface of $Co(OH)_2$ nanowires. Concurrently, the redundant S ions released from $(NH_4)_2MoS_4$ reacted with $Co(OH)_2$ nanowires to form porous CoS_2 nanowires which served as structural backbones to guide the growth of MoS_2 nanosheets. SEM studies showed that the MoS_2/CoS_2 nanowires grew vertically and densely on CC (inset to Fig. 1a) and the MoS_2/CoS_2 nanowires exhibited a diameter of *ca.* 500 nm and a length of 3 to 5 μm (Fig. 1a). In fact, higher-magnification SEM measurements showed a uniform coverage of interconnected MoS_2 nanosheets on the entire CoS_2 nanowires (Fig. 1b). By contrast, CoS_2/CC exhibited only CoS_2 hollow nanotubes with diameters of about 500 nm (Fig. 1c), and in MoS_2/CC only MoS_2 nanosheets can be seen (Fig. 1d).

Fig. 1e depicts the XRD patterns of MoS_2/CoS_2/CC. One can see four sharp peaks at 2θ = 32.3, 36.2, 39.8 and 55.1° which

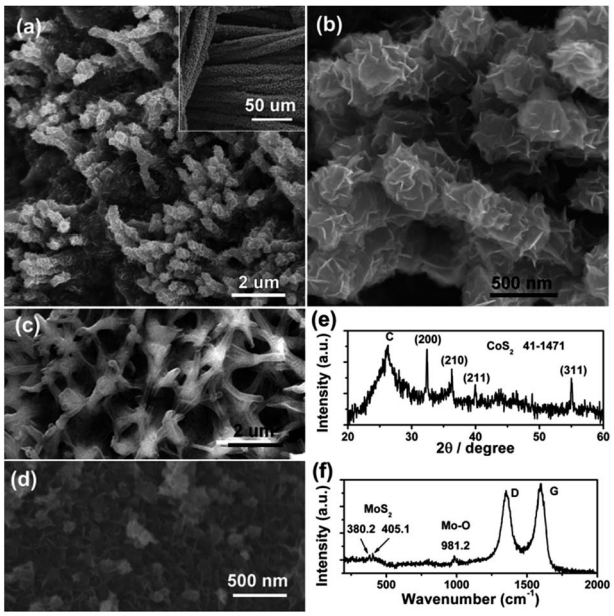

Fig. 1 SEM images of (a and b) MoS_2/CoS_2/CC, (c) CoS_2/CC and (d) MoS_2/CC. (e) XRD patterns and (f) Raman spectrum of MoS_2/CoS_2/CC. The inset to (a) is an SEM image of MoS_2/CoS_2/CC at low magnification.

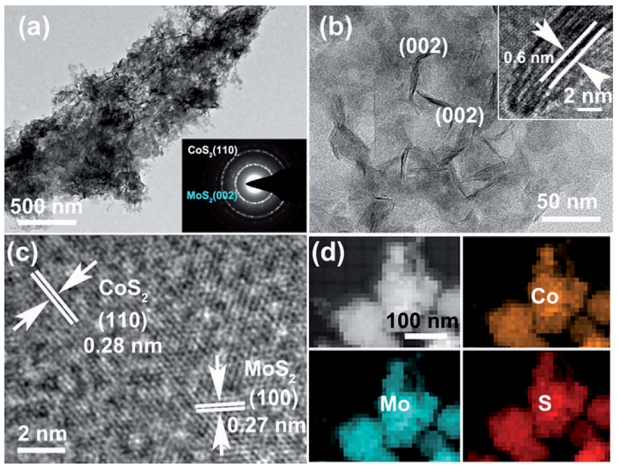

Fig. 2 (a–c) Representative TEM images of MoS_2/CoS_2. The inset to (a) is the selected area electron diffraction patterns of MoS_2/CoS_2; and inset to panel (b) is a high-resolution TEM image of MoS_2/CoS_2. (d) The corresponding EDX elemental mapping images of Mo, Co and S for MoS_2/CoS_2.

correspond to the (200), (210), (211), and (311) planes of CoS_2 (JCPDS no. 41-1471). The broad diffraction peaks at $2\theta = 26.2^\circ$ arise from the CC substrate. No diffraction peak of MoS_2 can be detected, possibly due to a low content and a small thickness of only a few layers. However, Raman measurements (Fig. 1f) of MoS_2/CoS_2/CC show two peaks at 380.2 and 405.1 cm^{-1} which are characteristic of MoS_2, confirming the formation of MoS_2. Note that the peak positions are similar to those of Li-doped 1T-MoS_2,[21] possibly due to Co-doping or the formation of MoS_2/CoS_2 heterostructures. In addition, the vibrational band at 981.2 cm^{-1} suggested the formation of Mo–O bonds,[21,31] implying the doping of O into MoS_2 during the decomposition of $Co(OH)_2$. The peaks at 1350.4 and 1593.8 cm^{-1} are characteristic of the D and G vibrational bands of the graphitic CC substrate.

The structure and morphology of MoS_2/CoS_2 were further investigated by (HR)TEM measurements. Fig. 2a shows a typical TEM image of an individual CoS_2 nanowire covered by thin MoS_2 nanosheets. The MoS_2 nanosheets were about 10 nm thick and grown tightly on the CoS_2 nanowire surface. It should be noted that the CoS_2 nanowires possessed a porous structure during the reaction between $(NH_4)_2MoS_4$ and $Co(OH)_2$. Thus, the interface between the CoS_2 backbone and the MoS_2 shell is difficult to identify. In the TEM image in Fig. 2b, the layered structures of MoS_2 nanosheets can be clearly seen with an interlayer distance of 0.62 nm that is consistent with the MoS_2 (002) crystalline planes (inset to Fig. 2b). In Fig. 2c, one can see well-defined lattice fringes with a spacing of 0.27–0.28 nm, which is consistent with both CoS_2 (110) (0.28 nm) and MoS_2 (100) (0.27 nm). The coexistence of CoS_2 and MoS_2 was also manifested by the diffraction rings in the selected area electron diffraction (SAED) patterns (inset to Fig. 2a). Notably, the similar interplanar spacing between CoS_2 (110) and MoS_2 (100) suggests good lattice matching, which might be beneficial in the formation of a strong heterogeneous structure.[40,41] In fact, elemental mapping studies confirmed the intimate contact between CoS_2 and MoS_2 in MoS_2/CoS_2 with a homogeneous distribution of the S element (Fig. 2d). Additionally, it revealed the co-existence of the Co element within MoS_2, in spite of the relatively low content. This suggests the formation of Co-doped MoS_2.

XPS measurements are then carried out to evaluate the chemical compositions as well as elemental valence states. The survey spectrum in Fig. 3a confirms the presence of Co, Mo, S, C and O elements in MoS_2/CoS_2/CC. From the high-resolution scan in Fig. 3b, the Mo 3d spectrum may be deconvoluted into two peaks at 228.3 and 231.8 eV. In addition, the characteristic

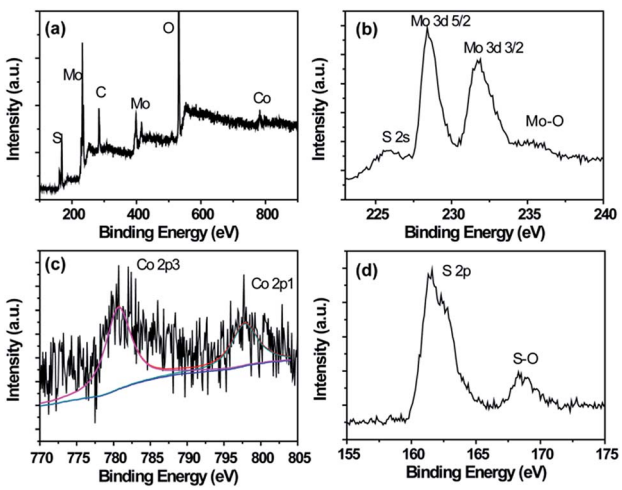

Fig. 3 (a) XPS survey spectrum and high-resolution scans of (b) Mo 3d, (c) Co 2p and (d) S 2p electrons of MoS_2/CoS_2/CC. Black curves are experimental data and colored curves are deconvolution fits.

peaks of Mo 3d in Mo–O and S 2p in S–O bonds can be observed at 235.3 and 168.6 eV in Fig. 3b and d, respectively, whereas the S 2p electrons in MoS_2 are manifested by the two peaks at 225.8 eV and 161.7 eV. These signify O-doping in MoS_2.[42,43] For the Co 2p electrons (Fig. 3c), two distinct peaks can be identified at 780.9 and 797.6 eV, which can be assigned to Co $2p_{3/2}$ and Co $2p_{1/2}$, respectively. Furthermore, based on the integrated peak areas of Co 2p and S–O, the atomic contents of Co and O in MoS_2 are estimated to be 0.8 and 4.9 at%, respectively.

Interestingly, the MoS_2/CoS_2/CC nanocomposites exhibited apparent HER activity in 0.5 M H_2SO_4. Experimentally, MoS_2/CoS_2/CC was used directly as an electrode without a binding agent or conducting additive. The iR-uncorrected polarization curves in Fig. 4a show that the MoS_2/CoS_2/CC electrode exhibited a much better HER performance than CoS_2/CC and MoS_2/CC. For instance, at 10 mA cm^{-2}, the overpotential of MoS_2/CoS_2/CC was −87 mV, markedly smaller than those of CoS_2/CC (−288 mV) and MoS_2/CC (−155 mV). The enhanced HER activity of MoS_2/CoS_2/CC might be ascribed to the synergistic effects between CoS_2 and MoS_2.

The Tafel slopes of the various samples were then analyzed and compared (Fig. 4b), by fitting the linear portions of the polarization curves with the Tafel equation ($\eta = b \log j + a$),

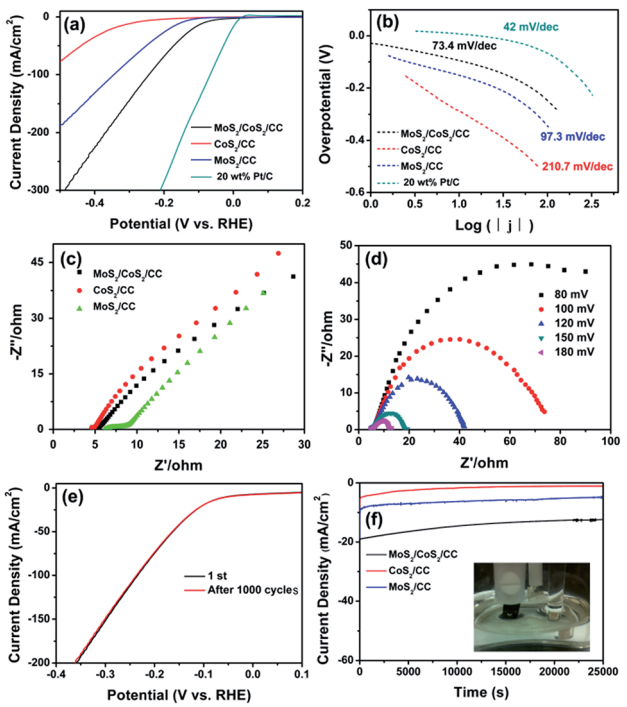

Fig. 4 (a) Polarization curves for HER in 0.5 M H_2SO_4 at MoS_2/CoS_2/CC, CoS_2/CC, MoS_2/CC and 20 wt% Pt/C on CC. Potential sweep rate 5 mV s^{-1}. (b) Corresponding Tafel plots derived from (a). (c) Nyquist plots of MoS_2/CoS_2/CC, CoS_2/CC, and MoS_2/CC at open-circuit potentials. (d) Nyquist plots of MoS_2/CoS_2/CC at various HER overpotentials in 0.5 M H_2SO_4. (e) HER polarization curves of MoS_2/CoS_2/CC before and after 1000 cycles in the stability test. (f) Current–time plots of the MoS_2/CoS_2/CC, CoS_2/CC and MoS_2/CC electrodes at the applied potential of −0.15 V (*vs.* RHE). Inset shows the generation of hydrogen bubbles on the electrode surface.

where j is the current density and b is the Tafel slope. The Tafel slope of MoS_2/CoS_2/CC is estimated to be 73.4 mV dec^{-1}, which is drastically lower than those of other samples, for example, MoS_2/CC (97.3 mV dec^{-1}) and CoS_2/CC (210.7 mV dec^{-1}), but higher than that of the 20 wt% Pt/C (42 mV dec^{-1}). A lower Tafel slope typically corresponds to more favorable HER kinetics, further confirming the synergistic contribution of the CoS_2 and MoS_2. EIS measurements were then carried out to further probe the electron-transfer kinetics involved. As shown in the Nyquist plots (Fig. 4c), the uncompensated resistance (R_s) for MoS_2/CoS_2/CC is small, less than 5.2 Ω, close to that of CoS_2/CC (4.5 Ω), but lower than that of MoS_2/CC (6.3 Ω). The results confirm that CoS_2 possessed high conductivity due to the metal-like conductivity property. Additionally, the charge transfer resistance (R_{ct}) diminished markedly with increasing overpotential from 126 Ω at −80 mV to 4.3 Ω at −180 mV, suggesting enhanced electron-transfer kinetics with increasing overpotentials, as depicted in Fig. 4d.

In addition to excellent catalytic activity, MoS_2/CoS_2/CC also exhibited extraordinary stability in acidic solution. Fig. 4e depicts the polarization curves of MoS_2/CoS_2/CC before and after the stability tests of 1000 potential cycles, where the current density remained virtually unchanged. Moreover, after 25 000 s' continuous operation at the applied potential of −0.15 V (*vs.* RHE), the current density of MoS_2/CoS_2/CC remained virtually invariant, once again confirming the remarkable HER stability in 0.5 M H_2SO_4 solution (Fig. 4f). In addition, one can see that the current density of the MoS_2/CoS_2/CC electrode was markedly larger than those of CoS_2/CC and MoS_2/CC at the same applied potential. The generation of hydrogen was confirmed by GC analysis (and manifested by the generation of hydrogen bubbles on the electrode surface, as depicted in Fig. 4f inset), which was quantitatively consistent with those estimated from *i–t* data (Fig. S2†). The faradaic efficiency (FE) was calculated by comparing the amount of experimentally quantified hydrogen with the theoretical value, which was 89.3% for CoS_2/CC, 100% for MoS_2/CC, and 96.8% for MoS_2/CoS_2/CC. This suggests that MoS_2 can improve the catalytic stability of CoS_2. After *i–t* testing, the morphologies of MoS_2/CoS_2/CC displayed no apparent changes, which confirmed the strong structural stability of the hybrid electrodes (Fig. S3†).

It should be noted that such an HER performance of MoS_2/CoS_2/CC (−87 mV *vs.* RHE at 10 mA cm^{-2}, Tafel slope of 73.4 mV dec^{-1}, and excellent catalytic stability) is better than or at least comparable to those of the MoS_2 or CoS_2-based HER electrocatalysts in acidic solution (Table S1†), for instance, metallic CoS_2 nanostructures (−148 mV *vs.* RHE at 10 mA cm^{-2}, and a Tafel slope of 51.6 mV dec^{-1}),[39] metallic CoS_2 nanopyramid arrays (−67 mV *vs.* RHE at 10 mA cm^{-2}, and a Tafel slope of 70.1 mV dec^{-1}),[44] Li-doped MoS_2/CC (−118 mV *vs.* RHE at 10 mA cm^{-2}, iR-corrected, and a Tafel slope of 62 mV dec^{-1}),[33] N-doped carbon-coated cobalt nanorod arrays on a titanium mesh (−106 mV *vs.* RHE at 10 mA cm^{-2}, and Tafel slope of 78.2 mV dec^{-1}),[36] *etc.*

The remarkable HER performance of the MoS_2/CoS_2 hierarchical arrays observed above might be rationalized as follows: (1) the high conductivity of the CC substrate and the metal-like

CoS_2 facilitated electron transport during hydrogen evolution; (2) the 3D hierarchical structure of the MoS_2/CoS_2 arrays exhibited a high electrochemically active surface area with abundant active sites (double-layer capacitance 7.04 mF cm^{-2}, Fig. S4†);[43] (3) doping by Co and O into MoS_2 produced abundant defect sites that served as catalytically active sites for the HER, as suggested by Raman spectroscopy and HRTEM measurements (Fig. 1f and 2); and (4) synergetic interactions between CoS_2 and MoS_2 at the interface induced electron transfer between Co and Mo, leading to enhanced electrocatalytic activity.[45]

Conclusions

In this study, a nanocomposite based on MoS_2 nanosheet-coated CoS_2 nanowire arrays supported on carbon cloth (MoS_2/CoS_2/CC) was prepared by a two-step procedure that entailed hydrothermal growth of a $Co(OH)_2$ nanowire array on carbon cloth followed by reaction with $(NH_4)_2MoS_4$ to obtain the MoS_2/CoS_2 composite structure. Electrochemical studies showed that the obtained 3D electrode exhibited excellent HER activity with an overpotential of −87 mV at 10 mA cm^{-2}, a small Tafel slope of 73.4 mV dec^{-1} and prominent electrochemical durability. The high HER performance was mainly attributed to the synergistic effects of co-doping of Co and O into MoS_2 nanosheets and hence the formation of structural defects, good conductivity of metallic CoS_2, and high electrochemically active surface area of the hierarchical 3D structure. The results presented herein may offer a new methodology for the design and engineering of effective HER catalysts based on earth-abundant and inexpensive components.

Acknowledgements

This work was supported by the National Recruitment Program of Global Experts, Zhujiang New Stars of Science & Technology (2014J2200061), Project of Public Interest Research and Capacity Building of Guangdong Province (2014A010106005), Fundamental Research Funds for the Central Universities (D2153880), National Natural Science Foundation of China (51502096), National Science Fund for Excellent Young Scholars of China (51422203), and Excellent Youth Foundation of Guangdong Scientific Committee (S2013050013882).

Notes and references

1 J. Yang and H. S. Shin, *J. Mater. Chem. A*, 2014, **2**, 5979–5985.
2 J. R. McKone, N. S. Lewis and H. B. Gray, *Chem. Mater.*, 2014, **26**, 407–414.
3 J. Luo, J.-H. Im, M. T. Mayer, M. Schreier, M. K. Nazeeruddin, N.-G. Park, S. D. Tilley, H. J. Fan and M. Grätzel, *Science*, 2014, **345**, 1593–1596.
4 S. Bai, C. Wang, M. Deng, M. Gong, Y. Bai, J. Jiang and Y. Xiong, *Angew. Chem., Int. Ed.*, 2014, **53**, 12120–12124.
5 R. Subbaraman, D. Tripkovic, D. Strmcnik, K.-C. Chang, M. Uchimura, A. P. Paulikas, V. Stamenkovic and N. M. Markovic, *Science*, 2011, **334**, 1256–1260.
6 I. E. L. Stephens and I. Chorkendorff, *Angew. Chem., Int. Ed.*, 2011, **50**, 1476–1477.
7 D. Hou, W. Zhou, X. Liu, K. Zhou, J. Xie, G. Li and S. Chen, *Electrochim. Acta*, 2015, **166**, 26–31.
8 S. Peng, L. Li, X. Han, W. Sun, M. Srinivasan, S. G. Mhaisalkar, F. Cheng, Q. Yan, J. Chen and S. Ramakrishna, *Angew. Chem., Int. Ed.*, 2014, **53**, 12594–12599.
9 Y. Yang, H. Fei, G. Ruan, C. Xiang and J. M. Tour, *Adv. Mater.*, 2014, **26**, 8163–8168.
10 M. S. Faber, M. A. Lukowski, Q. Ding, N. S. Kaiser and S. Jin, *J. Phys. Chem. C*, 2014, **118**, 21347–21356.
11 Y. Sun, C. Liu, D. C. Grauer, J. Yano, J. R. Long, P. Yang and C. J. Chang, *J. Am. Chem. Soc.*, 2013, **135**, 17699–17702.
12 D. Kong, H. Wang, Z. Lu and Y. Cui, *J. Am. Chem. Soc.*, 2014, **136**, 4897–4900.
13 X. Fan, H. Zhou and X. Guo, *ACS Nano*, 2015, **9**, 5125–5134.
14 L. Liao, S. Wang, J. Xiao, X. Bian, Y. Zhang, M. D. Scanlon, X. Hu, Y. Tang, B. Liu and H. H. Girault, *Energy Environ. Sci.*, 2014, **7**, 387–392.
15 H. B. Wu, B. Y. Xia, L. Yu, X.-Y. Yu and X. W. Lou, *Nat. Commun.*, 2015, **6**, 6512.
16 E. J. Popczun, J. R. McKone, C. G. Read, A. J. Biacchi, A. M. Wiltrout, N. S. Lewis and R. E. Schaak, *J. Am. Chem. Soc.*, 2013, **135**, 9267–9270.
17 Z. Xing, Q. Liu, A. M. Asiri and X. Sun, *Adv. Mater.*, 2014, **26**, 5702–5707.
18 S. Gu, H. Du, A. M. Asiri, X. Sun and C. M. Li, *Phys. Chem. Chem. Phys.*, 2014, **16**, 16909–16913.
19 P. Jiang, Q. Liu, C. Ge, W. Cui, Z. Pu, A. M. Asiri and X. Sun, *J.Mater. Chem. A*, 2014, **2**, 14634–14640.
20 Q. Liu, J. Tian, W. Cui, P. Jiang, N. Cheng, A. M. Asiri and X. Sun, *Angew. Chem., Int. Ed.*, 2014, **126**, 6828–6832.
21 M. A. Lukowski, A. S. Daniel, F. Meng, A. Forticaux, L. Li and S. Jin, *J. Am. Chem. Soc.*, 2013, **135**, 10274–10277.
22 D. Voiry, M. Salehi, R. Silva, T. Fujita, M. Chen, T. Asefa, V. B. Shenoy, G. Eda and M. Chhowalla, *Nano Lett.*, 2013, **13**, 6222–6227.
23 J. Duan, S. Chen, M. Jaroniec and S. Z. Qiao, *ACS Nano*, 2015, **9**, 931–940.
24 L. Yang, W. Zhou, D. Hou, K. Zhou, G. Li, Z. Tang, L. Li and S. Chen, *Nanoscale*, 2015, **7**, 5203–5208.
25 S. Chen, J. Duan, Y. Tang, B. Jin and S. Zhang Qiao, *Nano Energy*, 2015, **11**, 11–18.
26 D. Merki, S. Fierro, H. Vrubel and X. Hu, *Chem. Sci.*, 2011, **2**, 1262–1267.
27 H. Wang, Z. Lu, S. Xu, D. Kong, J. J. Cha, G. Zheng, P.-C. Hsu, K. Yan, D. Bradshaw and F. B. Prinz, *Proc. Int. Acad. Ecol. Environ. Sci.*, 2013, **110**, 19701–19706.
28 J. D. Benck, Z. Chen, L. Y. Kuritzky, A. J. Forman and T. F. Jaramillo, *ACS Catal.*, 2012, **2**, 1916–1923.
29 D. Merki, H. Vrubel, L. Rovelli, S. Fierro and X. Hu, *Chem. Sci.*, 2012, **3**, 2515–2525.
30 J. Xie, J. Zhang, S. Li, F. Grote, X. Zhang, H. Zhang, R. Wang, Y. Lei, B. Pan and Y. Xie, *J. Am. Chem. Soc.*, 2013, **135**, 17881–17888.

31 W. Zhou, D. Hou, Y. Sang, S. Yao, J. Zhou, G. Li, L. Li, H. Liu and S. Chen, *J. Mater. Chem. A*, 2014, **2**, 11358–11364.
32 W. J. Zhou, Y. H. Leng, D. M. Hou, H. D. Li, L. G. Li, G. Q. Li, H. Liu and S. W. Chen, *Nanoscale*, 2014, **6**, 4698–4704.
33 H. Wang, Z. Lu, D. Kong, J. Sun, T. M. Hymel and Y. Cui, *ACS Nano*, 2014, **8**, 4940–4947.
34 Q. Ding, F. Meng, C. R. English, M. Cabán-Acevedo, M. J. Shearer, D. Liang, A. S. Daniel, R. J. Hamers and S. Jin, *J. Am. Chem. Soc.*, 2014, **136**, 8504–8507.
35 D.-Y. Wang, M. Gong, H.-L. Chou, C.-J. Pan, H.-A. Chen, Y. Wu, M.-C. Lin, M. Guan, J. Yang, C.-W. Chen, Y.-L. Wang, B.-J. Hwang, C.-C. Chen and H. Dai, *J. Am. Chem. Soc.*, 2015, **137**, 1587–1592.
36 W. Zhou, Y. Zhou, L. Yang, J. Huang, Y. Ke, K. Zhou, L. Li and S. Chen, *J. Mater. Chem. A*, 2015, **3**, 1915–1919.
37 W. Zhou, X.-J. Wu, X. Cao, X. Huang, C. Tan, J. Tian, H. Liu, J. Wang and H. Zhang, *Energy Environ. Sci.*, 2013, **6**, 2921–2924.
38 P. Jiang, Q. Liu, Y. Liang, J. Tian, A. M. Asiri and X. Sun, *Angew. Chem., Int. Ed.*, 2014, **53**, 12855–12859.
39 M. S. Faber, R. Dziedzic, M. A. Lukowski, N. S. Kaiser, Q. Ding and S. Jin, *J. Am. Chem. Soc.*, 2014, **136**, 10053–10061.
40 W. Zhou, H. Liu, J. Wang, D. Liu, G. Du and J. Cui, *ACS Appl. Mater. Interfaces*, 2010, **2**, 2385–2392.
41 W. Zhou, Z. Yin, Y. Du, X. Huang, Z. Zeng, Z. Fan, H. Liu, J. Wang and H. Zhang, *Small*, 2013, **9**, 140–147.
42 Z. Chen, D. Cummins, B. N. Reinecke, E. Clark, M. K. Sunkara and T. F. Jaramillo, *Nano Lett.*, 2011, **11**, 4168–4175.
43 X. Liu, W. Zhou, L. Yang, L. Li, Z. Zhang, Y. Ke and S. Chen, *J. Mater. Chem. A*, 2015, **3**, 8840–8846.
44 W. A. Bhutto, Z. Wu, Y. Cao, W. Wang, J. He, Q. Luo, S. Li, H. Li and J. Kang, *J. Mater. Chem. A*, 2015, **3**, 6360–6365.
45 H. Zhu, J. Zhang, R. Yanzhang, M. Du, Q. Wang, G. Gao, J. Wu, G. Wu, M. Zhang and B. Liu, *Adv. Mater.*, 2015, **27**, 4752–4759.